

Electron temperature, ion density and energy influx measurements in a tubular plasma reactor for powder surface modification

This content has been downloaded from IOPscience. Please scroll down to see the full text.

2012 J. Phys. D: Appl. Phys. 45 355202

(<http://iopscience.iop.org/0022-3727/45/35/355202>)

View [the table of contents for this issue](#), or go to the [journal homepage](#) for more

Download details:

IP Address: 136.206.1.12

This content was downloaded on 05/04/2015 at 11:43

Please note that [terms and conditions apply](#).

Electron temperature, ion density and energy influx measurements in a tubular plasma reactor for powder surface modification

C Roth, G Oberbossel and P Rudolf von Rohr¹

ETH Zurich, Institute of Process Engineering, Sonneggstrasse 3, 8092 Zurich, Switzerland

E-mail: roth@ipe.mavt.ethz.ch, oberbossel@ipe.mavt.ethz.ch and vonrohr@ipe.mavt.ethz.ch

Received 12 April 2012, in final form 20 June 2012

Published 14 August 2012

Online at stacks.iop.org/JPhysD/45/355202

Abstract

The tubular plasma reactor was designed for the continuous surface modification of fine powders in non-equilibrium RF discharges. So far, little has been known about the plasma characteristics of this inductively coupled reactor system. Therefore, moderate pressure argon–oxygen discharges, commonly used for powder processing, are investigated with tailor-made probe techniques. The influence of plasma power, system pressure, gas composition and mean gas velocity on the axial profiles of plasma parameters was studied. Electron temperature and positive ion density profiles were measured with a Langmuir double probe and the energy influx due to the plasma was determined by a new type of calorimetric probe. The limits for the E–H-mode transition are provided and photographs of the discharge are presented to illustrate the relationship between process parameters and plasma characteristics. Both, ion density and energy influx increased with rising plasma power. The axial energy influx profiles were in addition strongly influenced by the mean gas velocity. Based on these profiles the maximum transient particle temperature was calculated as a function of the particle diameter. Particle temperatures in the order of 100 °C were estimated, whereas the thermal load of the substrates rises with increasing plasma power, residence time and pressure.

(Some figures may appear in colour only in the online journal)

1. Introduction

Macroscopic powder properties such as wettability, dissolution rate, flowability, compactibility or sieving speed can be tuned in non-equilibrium plasmas to yield products with favourable characteristics. These effects are achieved by either depositing nanoparticles or nearly coherent films onto the substrate particles [1, 2] or by the formation of functional groups on the particle surface [3]. Argon–oxygen discharges are often used to create polar groups as –OH or –COOH, which are required to reduce the water contact angle. Thus, powders such as high-density polyethylene (HDPE) become wettable with water [3] or the dissolution time of pharmaceutical ingredients such as salicylic acid decreases [4].

A well-suited reactor concept for the continuous surface modification of powders at low and moderate pressure is the so-called tubular plasma reactor (TPR). It differs substantially from a classic low-pressure plasma chamber and basically consists of a long glass tube connected to a gas and powder feed unit at its top and to a gas–solid separation unit and a vacuum pump at its lower end. Under normal operation fine-grained powders pass the tube with high velocity and the particle surfaces are functionalized on their way through the discharge in approximately 0.1 s [5]. A variation of process parameters such as plasma power or process pressure primarily influences the plasma parameters such as ion density and electron temperature. These plasma physical conditions determine the degree of surface activation and thus, the powder properties after the treatment. Therefore, we measured some fundamental plasma parameters under process conditions

¹ Author to whom any correspondence should be addressed.

which are normally applied to modify powder surfaces in the TPR. The plasma physical description of this kind of plasma reactor requires special care since it features high mean gas velocities (up to 43 m s^{-1}), high specific power input (up to approximately 300 W l^{-1}), negative ions, inductive coupling and moderate pressures (up to 300 Pa). This parameter combination is seldom explored in plasma functionalization processes but nevertheless necessary for fast and effective modification of powder surface properties.

We were interested in the spatial profile of plasma parameters and direct optical access was not available. Hence, we used intrusive probe techniques to investigate the reactor. A Langmuir double probe was employed to determine the local electron temperature T_e and the positive ion density n_{i+} . A new type of calorimetric probe was designed and applied to measure the energy influx J_{in} originating from the plasma.

An inductive coupling ensures radial symmetry of plasma parameters in the tube, which is required for the homogeneous treatment of powder substrates. An inductively coupled plasma (ICP) can ignite either in E-mode (dominant capacitive coupling) or H-mode (dominant inductive coupling) [6]. The mode transition is not continuous and an abrupt change in charge carrier density and light emission by up to two orders of magnitude is observed [7]. Since the plasma parameters change step-wise from E- to H-mode, the prevailing discharge mode in the whole parameter field was determined before the probe measurements.

The Langmuir double probe was first introduced by Johnson and Malter [8]. Its two electrodes are electrically floating and require no reference potential. Therefore, this method is well suited to investigate the electrodeless radiofrequency (RF) plasma in the TPR where no reference potential is available [9, 10]. In general, a double probe draws less current from the plasma than a single probe since the total current to the probe can never exceed the positive ion current [8]. As a result, the discharge is disturbed less by the double probe method [10]. In addition, double probes are supposed to be more reliable in plasma devices with high magnetic fields, since the ion motion is less affected than the electron motion [11].

The calorimetric principle to measure the energy influx in a plasma was first reported by Thornton [12]. The transient temperature of a probe with known heat capacity is recorded during the heating cycle (plasma on) and the cooling cycle (plasma off). The cooling cycle is used to determine the temperature-dependent energy loss of the probe. During the heating cycle the sum of energy influx due to the plasma and energy loss (radiation, convection, and conduction) determines the probe temperature. Knowing the energy loss as a function of the probe temperature from the cooling cycle, this term can be subtracted from the measured total energy influx during the heating cycle at the respective temperature to obtain the energy influx due to the plasma. The energy influx represents the sum of all energy containing particle fluxes towards the probe as well as surface reactions. In general the energy influx is composed of the following components [13]:

- impact of energetic electrons, ions, neutrals and photons,
- positive ion–electron recombination on the surface,

- positive ion–negative ion recombination on the surface,
- association processes on the surface,
- exothermic reactions with the surface,
- relaxation of metastable states on the surface.

Since their introduction in 1978 calorimetric probes have been further developed and became an accepted plasma diagnostic to describe the thermal load of a substrate immersed in a non-equilibrium discharge. Measurements were performed in RF-plasmas [14], magnetrons [15], hollow cathode glow discharges for powder processing [16], or even atmospheric pressure plasma jets [17]. In addition, particles confined in a plasma have been used as micro-calorimetric probes [18]. Also, the various contributions to the energy influx and the different heat loss mechanisms were identified in plasma chambers with relatively low pressure, plasma power and mean gas velocity [19].

Fibre optic temperature sensors were directly used as calorimetric probes in a former, capacitively coupled version of the TPR [20]. Measurements have been performed at four radial positions in between the electrodes. The resulting radial energy influx profile showed significantly higher values in the tube centre compared with the positions close to the reactor wall. However, these measurements were limited to a plasma power of 75 W due to the polymeric nature of the sensors. The fibre optic probes were compared with a classic calorimetric probe [21] in the afterglow of the TPR [22]. Comparable energy influx values were achieved with both probes and the influence of plasma power, gas composition, system pressure, and total gas flow rate was studied. The energy influx in the afterglow rose with increasing plasma power, total gas flow rate, and argon concentration. Nevertheless, the measurements were limited to low power inputs and a measurement position downstream the discharge centre. The thermal stability of the fibre optic probes was insufficient and the conducting and grounded rod of the classic probe led to distortions of the discharge during measurements in the domain of the plasma source. In addition, the determination of the effective heat capacity of the probe head was found to be inaccurate for the fibre optic probes.

Therefore, a new calorimetric probe was designed for this study, which can withstand high temperatures, offers simple determination of the effective heat capacity, and is not influenced by the strong electromagnetic fields. This new probe allows one to measure the energy influx even in an ICP at process parameters suitable for powder processing. Thereby the working range of this plasma diagnostic was expanded and it was for the first time possible to determine the thermal load of particle substrates during the surface modification in the TPR as a function of the process parameters.

In order to avoid probe contamination, no substrate powder or organosilicon monomer (required for the formation of films or nanoparticles) was fed to the reactor during the probe measurements and only Ar : O₂ mixtures were investigated. If substrate powder is supplied to the reactor the system needs to be described as dusty plasma and the discharge parameters are expected to vary significantly. Nevertheless, the qualitative influence of the process parameters on the plasma parameters

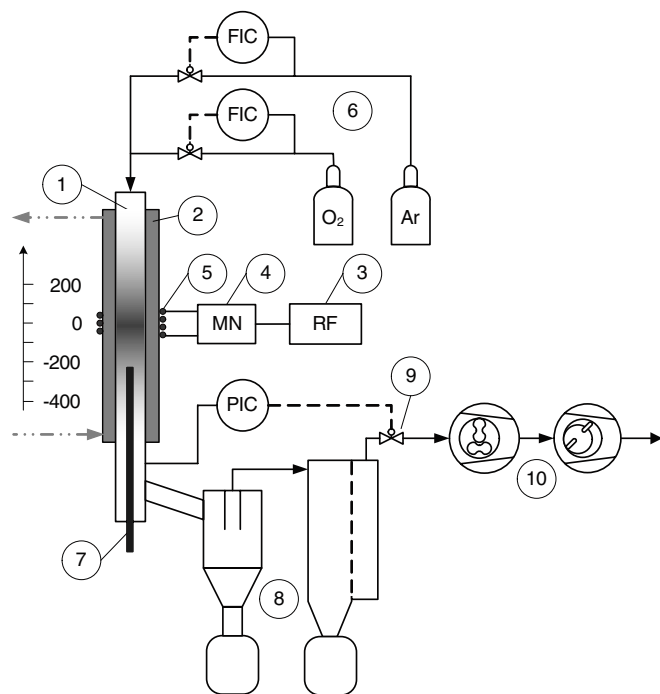


Figure 1. Principal sketch of the TPR and the probe coordinate system; FIC: flow indicator controller, PIC: pressure indicator controller, numbers are indicated in the text.

is expected to be similar in the more complex case of substrate powder admixture.

We intended to give some insights into the plasma parameters in the TPR under process conditions suitable for efficient powder processing. Such information was missing for many years and rendered the interpretation of powder-related results difficult. In the course of this investigation it became clear that this reactor system can be used to modify particles but also to study the fundamentals of discharges with significant flow effects. Hence, the presented measurements will also improve the general understanding of moderate pressure discharges at elevated gas flow rates and serve further applications in this parameter range.

2. Experimental

2.1. Tubular plasma reactor

The process scheme of the investigated TPR is shown in figure 1. The plasma chamber (1) consists of a 1.5 m long double wall glass reactor. The gap in between inner and outer tube was filled with deionized water (2) for temperature control. The cooling jacket temperature was kept constant at 20 °C for all experiments. The inner diameter of the reactor measures 40 mm. This results in an effective reactor volume of approximately 0.5 to 1.5 l depending on the expansion of the discharge within the glass tube.

The discharge was driven by an ICP source which operates at a RF of 13.56 MHz. The RF-generator (3) was connected via a matching network (MN) (4) to the water cooled copper coil (5) on the outside of the cooling jacket. The vertical distance between the coil and the upper flange measures 650 mm and

Table 1. Standard process conditions and parameter ranges.

Parameter	Standard conditions	Parameter range
Plasma Power	300 W	100–400 W
System Pressure	200 Pa	55–300 Pa
Total gas flow rate	1500 sccm	300–6000 sccm
Molar oxygen fraction	33.3%	0–100%

850 mm to the lower flange, respectively. The matchbox was always adjusted to minimize the reflected power. The flow rates of oxygen (purity >99.999%) and argon (purity >99.999%) were regulated by flow controllers (6). The radially centred probes (7) were inserted from the bottom or the top of the reactor and could be moved in the vertical direction. The used coordinate system for the measurement position is relative to the coil position (centre of the discharge) and positive against the flow direction (see figure 1). The gas mixture left the reactor through a cyclone and filter unit (8) at the lower end of the glass tube. A constant pressure in the reactor was maintained by a butterfly control valve (9) in front of the double stage vacuum pump (10).

In most low-pressure plasma chambers the total gas flow rate plays a minor role and primarily determines the overall system pressure. At sufficiently low pressure the statistics of single atoms and molecules are considered, known as the free molecular regime. However, the investigated pressure range in this study is classified into the intermediate regime and the flow pattern is no longer negligible. If the pressure was kept constant by means of the control valve (9) and the total gas flow rate was increased, the overall gas velocity increased as well. On the other hand, if the pressure was adjusted by the total gas flow rate (constant valve position), the residence time and mean gas velocity remained constant, but the specific energy per atom or molecule changed. In order to account for these linked parameters, the pressure was varied in two independent series to study its influence on the plasma parameters. The standard process conditions and the parameter ranges are summarized in table 1.

2.2. Determination of the E–H-mode transition

The hysteresis of the E–H-mode transition in an ICP was used to determine the dominant power coupling mechanism as a function of the process parameters. Above a certain pressure the mode transition passes a hysteresis [23], so that three distinct regions can be distinguished: The stable E-mode zone at low power, the hysteresis zone where either E- or H-mode is possible, and the stable H-mode zone at high plasma power [7]. The mode transition could be observed visually due to the much higher optical emission in H-mode, as schematically illustrated in figure 2.

2.3. Photographs of the discharge

Photos of the discharge were taken with a commercial reflex camera (Sony, Alpha 200) at a constant focal length of 18 mm and a sensor sensitivity of ISO 100. Within one picture series the aperture and exposure time were kept constant.

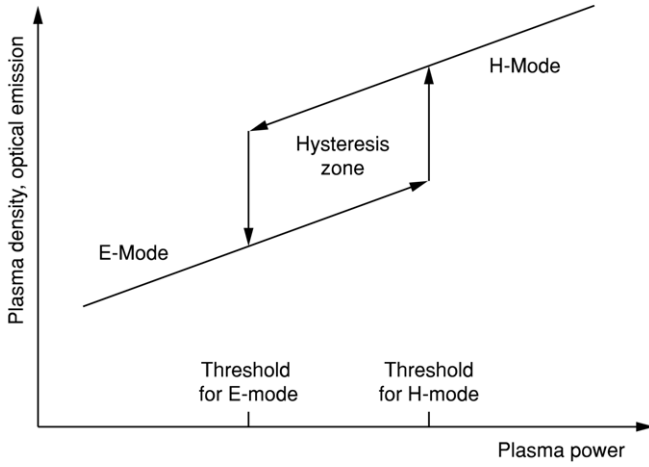


Figure 2. Schematic illustration of the E-H-mode transition.

2.4. Langmuir double probe

The Langmuir measurements were conducted with a home-made double probe, which withstands the harsh plasma environment and accounts for the low reactor cross-section. The probe head consisted of Macor, while all other parts were constructed of Al_2O_3 ceramics. The tungsten probe tips had a diameter of 0.3 mm, a height of 7 mm, and were arranged in parallel with a distance of 7 mm. Tungsten was chosen due to its high thermal stability and low secondary electron emission, which could be mistaken for an additional contribution to the positive ion current [24].

The current–voltage characteristic was recorded for each position and parameter setting 200 times with a resolution of 1000 voltage steps. For the acquisition of the current–voltage characteristic a commercial system (L2P, Plasma Consult, Germany) was used.

2.5. Calculation of electron temperature and positive ion density

We evaluated the measured current I as a function of the voltage V to determine the electron temperature T_e and the positive ion density n_{i+} . A typical characteristic is presented in figure 3 for standard conditions at the position 100 mm below the coil.

The characteristic is symmetric with respect to the origin, because the probe tip areas A_1 and A_2 were equal. For $V = 0$ both probe tips are at floating potential and the net current is equal to zero. For high voltages V the negative probe tip draws the positive ion saturation current I_{sat} from the discharge. A linear extrapolation of the measured current from the saturation region to $V = 0$ therefore leads to the positive ion saturation current, as illustrated in figure 3 and quoted in (1).

$$I_{\text{sat}} = \frac{I_{\text{sat1}}|_{V=0} + I_{\text{sat2}}|_{V=0}}{2}. \quad (1)$$

The electron temperature was determined from the slope of the characteristics at $V = 0$, corrected with the slope of the ion saturation current, as proposed in [25, 26] and shown

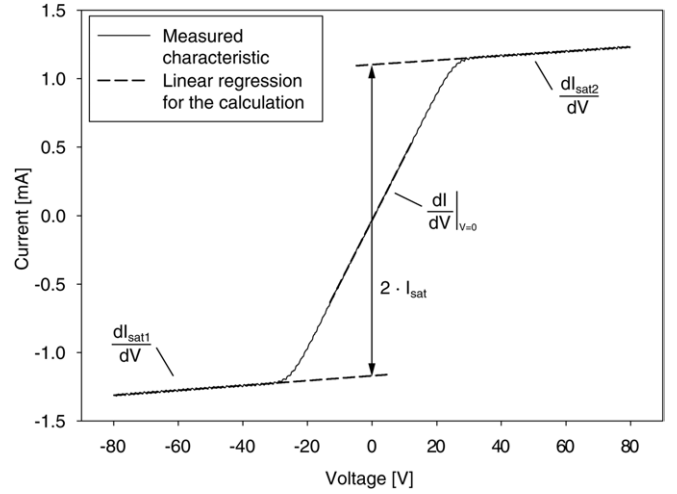


Figure 3. Typical current–voltage characteristic, acquired at the position 100 mm below the coil at a plasma power of 300 W, a pressure of 200 Pa, a molar oxygen fraction of 33.3% and a total gas flow rate of 1500 sccm.

in equation (2). k_B is the Boltzmann constant and e is the elementary charge.

$$\frac{k_B \cdot T_e}{e} = \frac{I_{\text{sat}}}{2 \cdot \left. \frac{dI}{dV} \right|_{V=0} - \frac{1}{2} \cdot \left(\frac{dI_{\text{sat1}}}{dV} + \frac{dI_{\text{sat2}}}{dV} \right)}. \quad (2)$$

The effect of collisions on the electron temperature determination is small, as long as the characteristics are evaluated around the floating potential [25, 27]. Double probes always float with respect to ground potential, so that this condition is fulfilled. A correction factor for the electron temperature due to collisions is introduced in [25] and always below 20% for double probes. This correction factor was estimated to be <3% for the investigated conditions and therefore, no correction was applied. Double probe characteristics are also relatively insensitive to negative ions as long as the ratio between negative ions and positive ions n_{i-}/n_{i+} is smaller than 0.99 [28, 29]. This condition is fulfilled up to an electronegativity ($\alpha = n_{i-}/n_e$) in the order of 100. In general, the electronegativity decreases with rising discharge power, process pressure, and argon content and is smaller than 1 under comparable discharge conditions [30, 31]. Hence, we suppose that the determination of the electron temperature was only slightly influenced by the presence of negative ions.

The mass has to be known for a proper determination of the positive ion density with a Langmuir probe. This requirement causes no problems for pure atomic gases where one ion species is predominant (single charged positive ions). However, in the case of molecular gases or gas mixtures the relative ion concentration must be known. Hence, in the investigated Ar:O₂ plasma various positive ions such as Ar^+ , Ar^{2+} , O_2^+ or O^+ should be considered for a proper determination of the positive ion density. Since the individual ion concentrations could not be measured, we calculated the positive ion density only in a qualitative manner as outlined

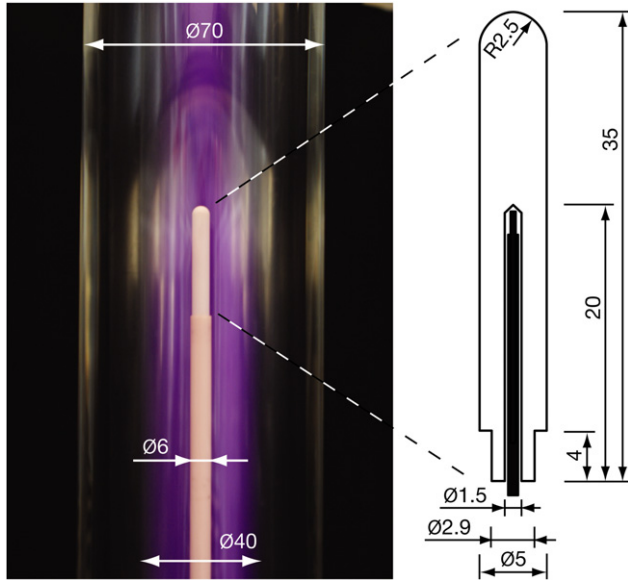


Figure 4. Calorimetric probe in the TPR with a cross-section sketch of the probe head.

in (3), by considering only one type of positively charged ions.

$$n_{i+} = \frac{I_{\text{sat}}}{A_{\text{pr}} \cdot e \cdot \sqrt{\frac{k_B \cdot T_e}{m_i}}}, \quad (3)$$

where A_{pr} is the probe area, and m_i is the ion mass. For mixtures of argon and oxygen the argon mass (40 u) and for pure oxygen discharges the mass of the oxygen molecule (32 u) was used for the calculation. The relative error originating from the unknown ion mass on the ion density determination is approximately 10%. Even though collisions in the sheath around the probe tips slightly decreased the electron and ion current no corrections were made, since the ion density was determined in a qualitative manner only.

For measurements downstream the coil position the Langmuir probe was inserted from the bottom. At measurement positions above the coil the characteristics were acquired by inserting the probe from the top. The central measurement point directly below the coil was averaged from the two measurement series.

2.6. Calorimetric probe

In an ideal case of a calorimetric measurement, the transient temperature of a thermally insulated, very small, chemically inert, and heat resistant substrate with known heat capacity and effective surface would be measured and evaluated. In reality such a situation cannot be reached but materials and geometries can be chosen in a way to limit heat conduction and fluid dynamic resistance to ease the determination of the effective heat capacity and surface.

We developed a new calorimetric probe according to these guidelines. It consists of a ceramic probe head with known heat capacity, an optical fibre to measure the probe head temperature, and a ceramic rod to position the probe head in the reactor. The probe head, pictured and sketched in figure 4, consists of alumina (Al_2O_3) which features a very high thermal

Table 2. Al_2O_3 probe head properties, the specific heat capacity at 45 °C is interpolated from values presented in [32].

Parameter	Value
Weight	2.251 g
Effective surface	486.95 mm ²
Specific heat capacity at 45 °C	814 J kg ⁻¹ K ⁻¹
Heat capacity	1.83 J K ⁻¹
Thermal conductivity	~ 30 W m ⁻¹ K ⁻¹

stability. It is an oxide ceramic and thus, does not alter within an oxygen-containing discharge as for instance metals, nitrides or carbides. The relevant material properties of the probe head are summarized in table 2.

In the central axis of the probe head a 1.5 mm diameter blind hole was manufactured. A commercially available fibre optic temperature sensor (TS2/3, Polytec GmbH, Germany) was glued into this hole using a highly heat conductive paste (ACHESON Silver DAG 1415, Plano GmbH, Germany). The fibre optic sensor itself consists of a fibre cable with a gallium arsenide (GaAs) crystal at its end. White light is conducted through the fibre and reflected at the crystal edge. Since the GaAs crystal has a temperature-dependent band edge displacement of 0.4 nm K⁻¹, the incident light is spectrally modified according to the crystal temperature. The reflected light was analysed with a spectrometer (FOTEMP-Multichannel, Polytec GmbH, Germany) and with the known relationship between temperature and GaAs band edge the temperature of the probe tip was determined [33]. The overall system accuracy according to the manufacturer is ± 2 °C.

The probe head with inserted optical fibre is plugged into an alumina rod of 6 mm outer diameter, which can be displaced along the central axis of the tubular reactor. The calorimetric probe was always inserted from the bottom of the reactor against the flow direction of the gas to keep the intrusive effect on the energy influx as low as possible. Due to the low thermal conductivity of the fibre cable and the nearly identical length specific heat capacity of the probe tip and the Al_2O_3 rod, the calorimetric probe head was considered as insulated. The probe head heat capacity of 1832 J K⁻¹ was determined by weighing the probe head and multiplying the weight with the known specific heat capacity. Hence, no error-prone calibration as in [20, 22] was necessary. The overall uncertainty of the probe head heat capacity is estimated to be within a small error frame of about 5%.

2.7. Calculation of the energy influx

The calculation method to determine the energy influx from the transient temperature curves corresponds exactly to our earlier study [22]. The main equation in calorimetric measurements is an energy balance over the probe head. The difference between the power input \dot{Q}_{in} and power losses \dot{Q}_{out} corresponds to the variation in probe enthalpy, which is the product of the mass m_{pr} , the specific heat capacity $c_{p,\text{pr}}$ and the derivative of the probe temperature T_{pr} , as given in (4).

$$m_{\text{pr}} \cdot c_{p,\text{pr}} \frac{dT_{\text{pr}}}{dt} = \dot{Q}_{\text{in}} - \dot{Q}_{\text{out}} = \int (J_{\text{in}} - J_{\text{out}}) dA = (J_{\text{in}} - J_{\text{out}}) \cdot A_{\text{pr}}. \quad (4)$$

Each power \dot{Q} is the surface integral over the energy flux J , which is in the case of a calorimetric probe the product of energy flux J and effective probe area A_{pr} . Every measurement comprises a heating phase (plasma on) and a cooling phase (plasma off) where the transient probe temperature is recorded. The change in probe enthalpy during the heating phase is proportional to the difference between the power input due to the plasma \dot{Q}_{in} (which is assumed to be temperature independent) and the temperature dependent heat loss $\dot{Q}_{out}(T_{pr})$.

$$\text{Plasma on : } m_{pr} \cdot c_{p,pr} \left(\frac{dT_{pr}}{dt} \right)_{\text{heat}} = \dot{Q}_{in} - \dot{Q}_{out}(T_{pr}). \quad (5)$$

The temperature-dependent heat loss (radiation, convection, etc) can be determined from the cooling phase. In this phase, the power input due to the plasma is equal to zero.

$$\text{Plasma off : } m_{pr} \cdot c_{p,pr} \left(\frac{dT_{pr}}{dt} \right)_{\text{cool}} = -\dot{Q}_{out}(T_{pr}). \quad (6)$$

Equation (6) has to be subtracted from equation (5) at the same probe temperature, to obtain the energy influx due to the plasma, as shown in (7).

$$J_{in} = \frac{\dot{Q}_{in}}{A_{pr}} = \frac{m_{pr} \cdot c_{p,pr}}{A_{pr}} \left[\left(\frac{dT_{pr}}{dt} \right)_{\text{heat}} - \left(\frac{dT_{pr}}{dt} \right)_{\text{cool}} \right]_{T_{pr}}. \quad (7)$$

During this study the heating phase was stopped as soon as the probe reached a temperature of 50 °C and the subsequent cooling phase was recorded. The transient heating and cooling phases between 40 and 50 °C were fitted by exponential functions and the temperature-dependent time derivatives were calculated. In a last step, equation (7) was evaluated between 40 and 50 °C with a resolution of 0.1 °C and averaged to obtain the energy influx due to the plasma.

3. Results and discussion

3.1. E–H-mode transition

In the investigated parameter range, specified in table 1, the E-mode prevailed as long as oxygen was admixed to the process gas. The upper power limit of the hysteresis zone (indicated in figure 2) was often not reached in the power domain up to 600 W. Hence, only the lower power limit of the hysteresis zone is shown as a function of the oxygen fraction in the process gas in figure 5 for three different pressure levels. The presented curve represents the maximum power that guarantees E-mode.

The E-mode threshold power rose with increasing oxygen concentration. Above 50% O₂, the hysteresis region could no longer be reached in the power domain below 600 W. Pure argon discharges ignited most readily in H-mode and the lower limit of the hysteresis zone nearly coincided with the extinction of the discharge. The E-mode threshold power rose as well with increasing pressure. This effect is already well described for pure oxygen discharges [34], where also the instabilities in the hysteresis zone were investigated in detail.

Not only gas concentration and pressure, but also the mean gas velocity influenced the lower limit of the E–H-mode transition region. We therefore varied the total gas flow rate

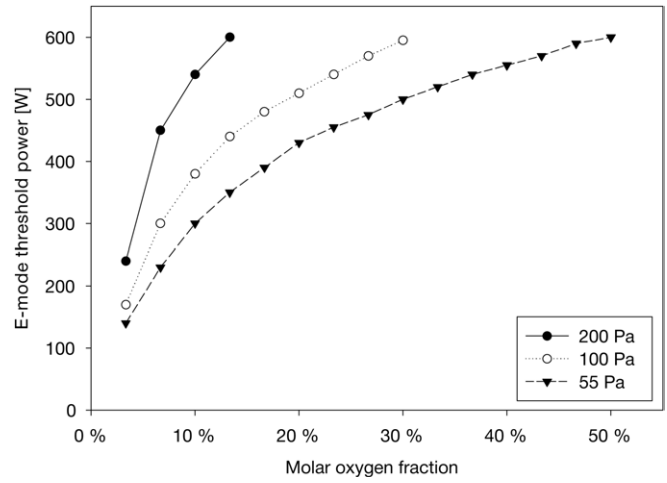


Figure 5. E-mode threshold power as a function of the molar oxygen fraction in the process gas for three pressure levels at a total gas flow rate of 1500 sccm.

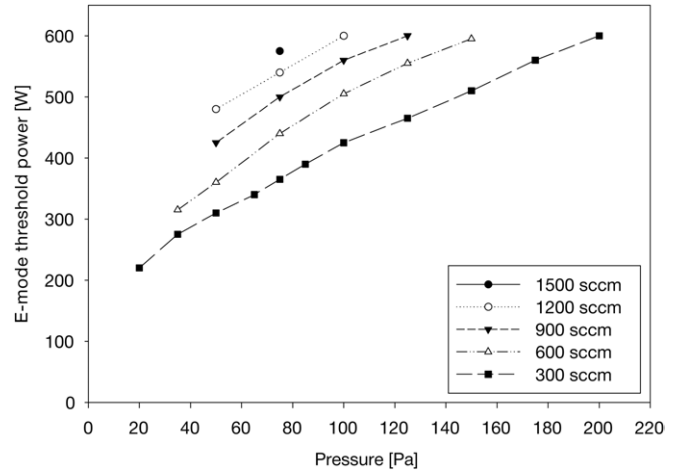


Figure 6. E-mode threshold power as a function of process pressure and total gas flow rate at a molar oxygen fraction of 33.3%.

and the pressure at a constant molar oxygen fraction of 33.3% as shown in figure 6.

The E-mode threshold power rose with increasing gas velocity and pressure. We assume that at elevated gas flow rates more charge carriers were lost at the lower end of the discharge. At the same time, the ionized gas was diluted more by neutrals at the upper boarder of the discharge. Thus, a higher discharge power was necessary to reach a critical plasma density where a transition to H-mode became possible.

We conclude from these measurements that within the pressure range for powder processing (100 to 300 Pa) and for total gas flow rates above 750 sccm, only E-mode is reached as long as the process gas contains at least a small quantity of oxygen. H-mode on the other hand is reached for pure argon or at very high plasma powers (which cannot be reached with the existing power supply) for Ar : O₂ mixtures.

3.2. Gas composition

The influence of different process gas ratios between argon and oxygen on the local distribution of plasma parameters

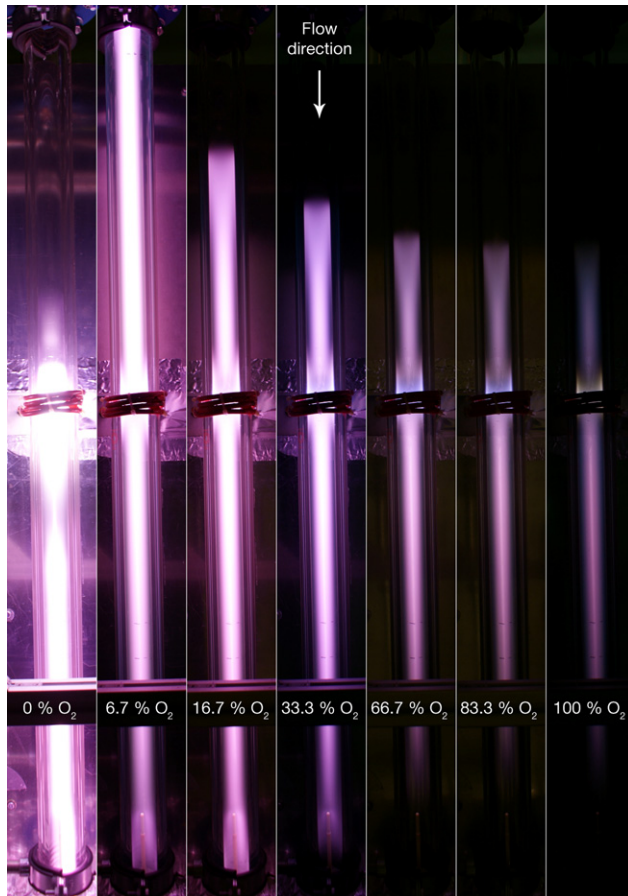


Figure 7. Photographs of the discharge as a function of the molar oxygen fraction for a plasma power of 300 W, a pressure of 200 Pa and a total gas flow rate of 1500 sccm. Photographs were taken with an aperture of 5 and an exposure time of 4 s.

was investigated first. We varied the oxygen fraction of the gas mixture at a constant plasma power of 300 W, a total gas flow rate of 1500 sccm and a system pressure of 200 Pa. The differences in optical emission, shown in figure 7, already indicate characteristic changes of the discharge as a function of the Ar:O₂ ratio.

Pure argon led to highly luminous H-mode plasma with maximum emission in the region of the inductive coil. The discharge switched to E-mode as soon as small quantities of oxygen (e.g. 6.7 vol%) were admixed. The transition was accompanied with a strong reduction in optical emission. The discharge was not confined in the glass tube at a low oxygen concentration of 6.7 vol%, but reached the upper and lower flange. With increasing oxygen fraction the discharge was first detached from the upper flange (e.g. at 16.7 vol% O₂) before it was fully confined within the glass tube (33.3 vol% O₂ and more).

In general, the optical emission decreased with rising oxygen fraction. Oxygen is known to quench excited argon states. In addition, the density of energetic electrons decreases if oxygen is admixed to argon [35, 36], such that the excitation of argon atoms becomes less probable [37]. Hence, the optical emission is reduced at increased oxygen fractions.

In figure 8 the axial electron temperature and positive ion density profiles are shown for a pure oxygen discharge and

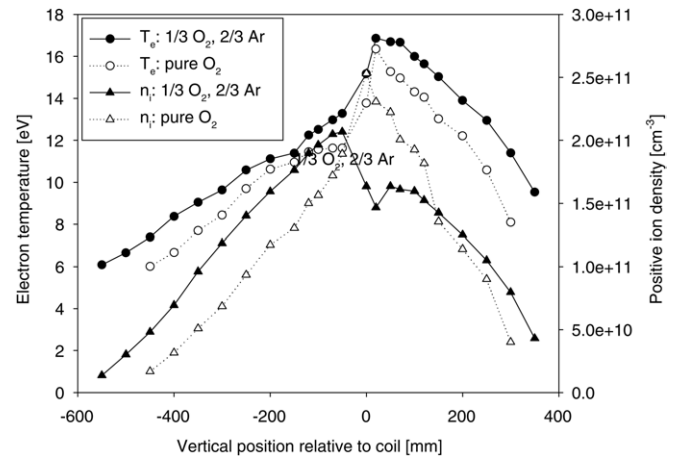


Figure 8. Axial electron temperature and positive ion density profiles as a function of the gas composition for a plasma power of 300 W, a pressure of 200 Pa and a total gas flow rate of 1500 sccm.

the Ar:O₂ mixture under standard conditions (see table 1). The intense H-mode ICP for pure argon could not be studied by the double probe method. The tungsten probe tips heated up substantially in the central region below the coil, causing massive errors or even probe damage.

The electron temperature profiles are very similar for both series with maximum values around 17 eV at the position of the helical coil and decreasing values up- and downstream the discharge centre. The electromagnetic field strength reaches its maximum in the domain of the inductive coil. The electrons are accelerated most in this region and lose their energy towards the upper and lower flange by collisions with gas particles or the wall. Hence, the general shape of the profiles along the glass tube is comprehensible. As a consequence of the axial electron temperature profiles we expect an increasing negative wall charge towards the position of the helical coil.

The absolute values of the measured electron temperatures are rather high compared with classic discharge systems in material processing at moderate pressures, where typical values between 1 and 10 eV are common [38]. On the one hand, only the high energy tail of the electron energy distribution function is evaluated and a Maxwellian distribution is presupposed in the analysis of the current-voltage characteristic of a Langmuir double probe measurement. Hence, the determined electron temperature could be slightly overestimated. On the other hand, a high electron temperature is required to sustain the plasma and to compensate the numerous losses at the reactor wall, if the surface-to-volume-ratio of a discharge system is large. The reactor diameter measures only 40 mm, which results in a high surface-to-volume-ratio of 100 m⁻¹. Plasma-wall interactions are therefore essential for this discharge system. In addition, the transmitted power was rather high, leading to power densities in the order of several hundred watts per litre. Hence, higher electron temperatures were reached in the central axis of the reactor compared with typical plasma-assisted material processing applications. Comparable electron temperatures in low-pressure reactors with similar dimensions are only found in magnetically enhanced discharges [39] or in plasmas operated in H-mode [40].

The electron temperature in Ar:O₂ plasmas normally increases for higher argon fractions due to the higher ionization energy of argon (15.76 eV) compared with atomic (13.61 eV) or molecular oxygen (12.06 eV) [41]. This effect was observed as well and slightly higher values were measured for the gas mixture compared with pure oxygen.

Since the local concentrations of different ion species are not known, the respective ion mass in equation (3) remains unknown. Hence, the comparison of ion density profiles for various oxygen concentrations in a quantitative manner is not meaningful within this study. Nevertheless, the two profiles in figure 8, including the uncertainty of the ion mass, show a characteristic difference in the region around the inductive coil. The ion density profile of the pure O₂ discharge peaks exactly at the axial position of the coil (0 mm) and follows the electron temperature profile. The profile of the Ar:O₂ mixture on the other hand passes a local minimum in the region of the inductive coil. A closer look at the discharge in the region of the coil is necessary to understand this phenomenon.

Since the discharge is operated in E-mode and at moderate pressure, different capacitive discharge forms can be distinguished: the weak-current α -regime and the strong-current γ -regime [42]. In the α -regime the first Townsend ionization coefficient dominates and heating is based on the displacement current in the plasma bulk. In the γ -regime secondary electron emission from the wall is intensified and the second Townsend ionization coefficient dominates. Thus, the heating primarily takes place in the sheath near the wall [43]. The α -regime is characterized by a low glow intensity and a smooth density distribution within the discharge. On the other hand, the γ -regime features several distinct zones comparable to a direct current glow discharge and a high optical emission near the wall. Under appropriate conditions the coexistence of both modes is also possible [42].

The oxygen discharge, shown in figure 7, featured generally low glow intensity. Apart from a very short zone around the helical coil, no optical emission was found along the wall. These properties are known from α -regime CCPs. In contrast to this, discharges with Ar:O₂ mixtures as process gas were much brighter with several distinct zones within the glass tube. Right below the coil an intense glow at the glass wall was observed, indicating strong secondary electron emission, while the region next to the wall was dark further up- and downstream. The probe measurements were performed in the central axis of the discharge tube. Along this axis the glow intensity was also not uniform in the case of Ar:O₂ mixtures and featured a local minimum in the domain of the inductive coil. We therefore suppose that the discharge of the gas mixture featured more γ -regime properties in the zone around the helical coil and transferred to an α -regime plasma further up- and downstream of the centre. On the other hand we assume that the first Townsend ionization coefficient dominated the heating process along the whole reactor in the pure oxygen discharge. Thus, a higher loss of positive ions to the walls in the region of the inductive coil connected with stronger secondary electron emission in the case of the Ar:O₂ discharge seems for us the most convincing explanation for the measured local drop of the positive ion density.

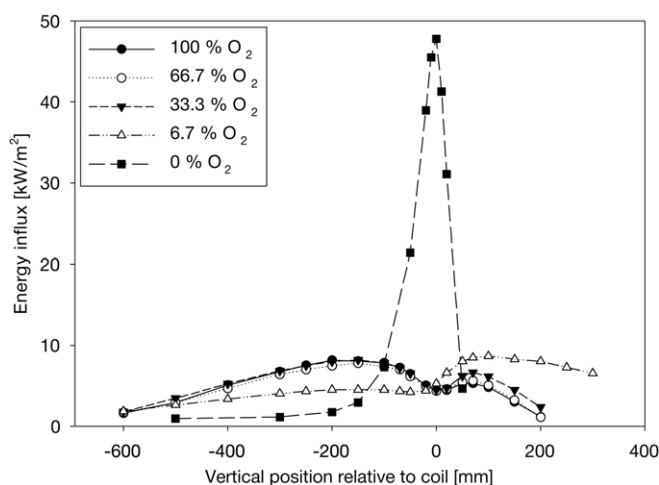


Figure 9. Axial energy influx profiles as a function of the molar oxygen fraction for a plasma power of 300 W, a pressure of 200 Pa and a total gas flow rate of 1500 sccm.

While only charged species can be studied with the Langmuir double probe, the energy influx measurements are strongly influenced by excited but uncharged particles. The contribution of impacts by electrons, photons and neutrals in the ground state is rather small at low gas temperatures. Reactions with the Al₂O₃ surface (i.e. oxidation) are also supposed to be unlikely at low probe temperatures. These reactions would primarily take place during the first exposure to the plasma and cause a systematic measurement error, which was not observed. The most important contributions to the total energy influx in the investigated process are the association of oxygen radicals, recombination reactions on the surface, relaxation of metastable states on the surface, and the impact of positive ions. Axial energy influx profiles as a function of the gas concentration are shown in figure 9 for a constant plasma power of 300 W, a pressure of 200 Pa and a total gas flow rate of 1500 sccm.

The most pronounced difference was found between the discharge of pure argon and argon–oxygen mixtures. Pure argon led to an intense H-mode discharge and featured a sharp peak in the domain of the inductive coil with energy influx values in the order of 50 kW m⁻². All mixtures of argon and oxygen as well as pure oxygen resulted in E-mode discharges, featuring much lower energy influxes. In addition, a characteristic local minimum in the axial profiles was found in the region of the helical coil for all oxygen-containing plasmas. Hence, for these gas mixtures the highest energy influx values were not measured in the discharge centre but about 150 to 200 mm below the position of the inductive coil. The series with the lowest oxygen fraction (6.7%) additionally showed an increased energy influx above the coil position. The discharge was not confined in the glass tube in this case but expanded into the upper flange, as visible in figure 7. This may have caused the higher energy influx in this region.

Impacts of charged species (positive ions, electrons, and negative ions) and its recombination are only responsible for a certain share of the total energy influx to the calorimetric probe. Therefore, the positive ion density profiles are only partially applicable to explain the measured energy influx propagations.

Even though no local minimum in the ion density profile of a pure oxygen discharge was found, the energy influx dropped significantly in the domain of the inductive coil. The measured profiles can only be understood by taking uncharged species into account as well. Fast neutrals, originating from ion–atom charge exchange collisions or elastic electron–atom collisions, and metastables, primarily produced by inelastic electron–atom collisions, can contribute significantly to the energy influx. In oxygen-containing plasmas neutral species were even found to be the main contribution to the energy influx [14]. Energetic neutrals are long-living species and not deflected by the electromagnetic field. Even though the energy transfer probability from excited atoms to amorphous oxide surfaces is very low [44], especially the argon metastable Ar^* plays an important role in argon–oxygen discharges [45]. The primary loss mechanism of Ar^* is the dissociation reaction of O_2 leading to an increased number of atomic oxygen. Oxygen radicals preferably recombine at surfaces such as the reactor wall or the calorimetric probe. The association of molecular oxygen to O_2 releases 5.16 eV and is one of the most important heating factors. Hence, metastables created in the region of the coil or above contributed to oxygen dissociation also far downstream from the discharge centre. A deformation of the axial profile into flow direction and a maximum energy influx downstream of the inductive coil in the case of $\text{Ar} : \text{O}_2$ mixtures are therefore comprehensible, by taking long-living neutral species into account as well.

The inner wall temperature below the coil was significantly increased compared with the rest of the tube due to the high negative charge and the consequent intense flux of positive ions towards the surface. The secondary electron emission, indicated by the photographs in figure 7, also suggests a high wall temperature in this domain. The probability for an association reaction of oxygen radicals is a strong function of the wall temperature and increases at elevated temperatures [46, 47]. Hence, we assume that the association of oxygen radicals to O_2 at the glass wall was increased in the region of the coil as well. The more radicals are lost at the hot wall, the fewer are available at the central reactor axis, where the energy influx measurements were performed. Thus, we suppose that a locally reduced oxygen radical concentration in the region of the helical coil decreased the energy influx at this position. This could explain why the pure oxygen discharge featured a local minimum in the energy influx profile, even though the ion density reached its maximum directly at this position.

The energy influx represents the sum of energetic particle fluxes towards the probe and surface reactions. Based on the presented measurements, a detailed split-up into the contribution of each energetic species and surface reaction is not possible. However, the measured axial profiles and the photographs suggest that both the impact of energetic ions as well as the recombination of oxygen radicals are the most decisive fractions of the energy influx.

3.3. Plasma power

We investigated the influence of the plasma power on the distribution of the plasma parameters along the reactor

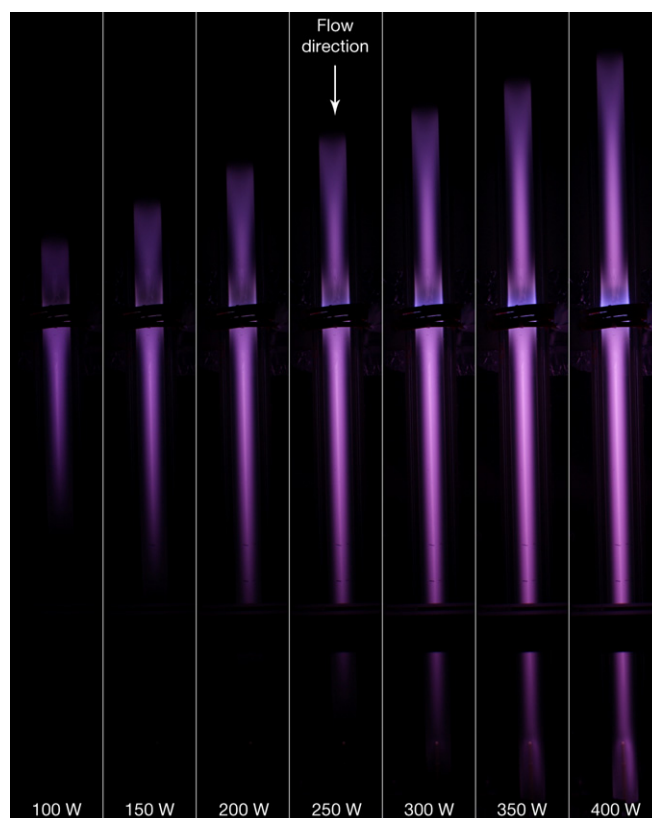


Figure 10. Photographs of the discharge as a function of the plasma power for a pressure of 200 Pa, a molar oxygen fraction of 33.3% and a total gas flow rate of 1500 sccm. Photographs were taken with an aperture of 5 and an exposure time of 0.6 s.

axis in a series with constant pressure (200 Pa), gas flow rate (1500 sccm), and gas concentration (1/3 O_2 , 2/3 Ar). Differences in the expansion and emission intensity of the discharge are visible in a series of photographs in figure 10.

In general, the glow intensity increased and the discharge expanded further up- and downstream with rising plasma power. The discharge propagated always further downstream than upstream due to the mean gas velocity of approximately 10.8 m s^{-1} . At the upper end of the discharge the plasma was rather uniform in radial direction and the sheath was very small. Further downstream towards the inductive coil the optical emission showed a necking towards the tube axis and a very low emission was found in the region next to the wall. We assume that this is a result of negative ions present in this domain. When a fluid element enters the discharge, electrons and positive ions are formed first. Electron attachment reactions lead then to the continuous formation of negative oxygen ions. Negative ions are contracted towards the discharge centre and reduce the flux of positive ions exiting the plasma [48, 49]. Hence, the glow intensity near the wall is reduced.

Further downstream, in the domain of the helical coil, the emission was intensified also near the wall, especially at elevated plasma power, indicating a strong emission of secondary electrons. Below the inductive coil the discharge was again contracted towards the tube axis and continuously lost intensity towards the lower end of the tube. Based on the

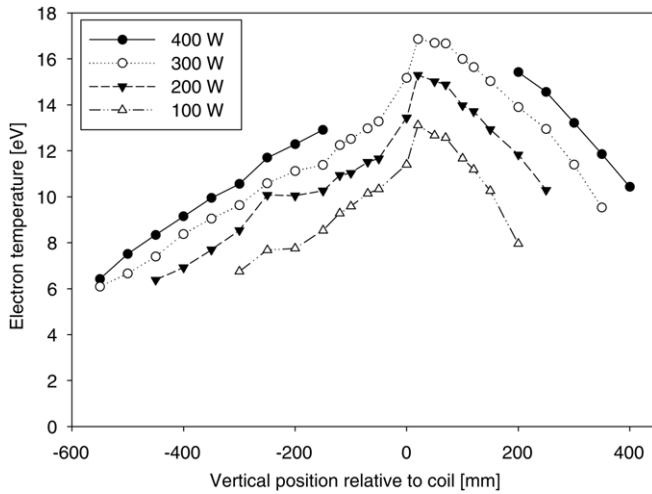


Figure 11. Axial electron temperature profiles as a function of the plasma power for a pressure of 200 Pa, a molar oxygen fraction of 33.3% and a total gas flow rate of 1500 sccm.

photographs we expect a volume dominated heating process according to the first Townsend coefficient up- and downstream the discharge centre. In the domain of the inductive coil both regimes (α and γ) have probably contributed to the heating. With increasing discharge power the emission near the walls around the helical coil was intensified, indicating an enhanced heating in the sheath and presheath region according to the second Townsend coefficient.

Axial electron temperature profiles as a function of the discharge power are shown in figure 11. For the highest investigated plasma power of 400 W no measurements were possible between 250 mm below and 200 mm above the coil. In this region the probe tips heated up substantially during the measurement.

The electron temperature rose with increasing plasma power and peaked at a position slightly above the coil centre. The discharge expanded further downstream than upstream, as already observed in the photographs. At the upper end of the discharge, higher electron temperatures were measured compared with the lower end. This finding stands in good correlation with the photographs, in which a sharp end of the emission was found at the upper edge of the discharge, whereas a fade-out of the emission was observed at the lower end. We believe that this is a result of the overall flow velocity, which is directed towards the lower end of the tube. Uncharged particles, such as metastables, are transported downstream where they contribute to dissociation reactions of oxygen or penning ionization. Hence, the discharge is enlarged towards the gas flow direction.

A similar shift was also observed in the positive ion density profiles shown in figure 12. The profiles are not perfectly symmetric with respect to the coil position. Equal ion density values are found about 100 mm further away from the coil when comparing the lower part of the discharge to the upper part. Penning ionization, being more pronounced downstream the centre, could explain this shift of the ion density profile.

It is generally known that the ion density scales with the transmitted plasma power [50]. However, the local minimum

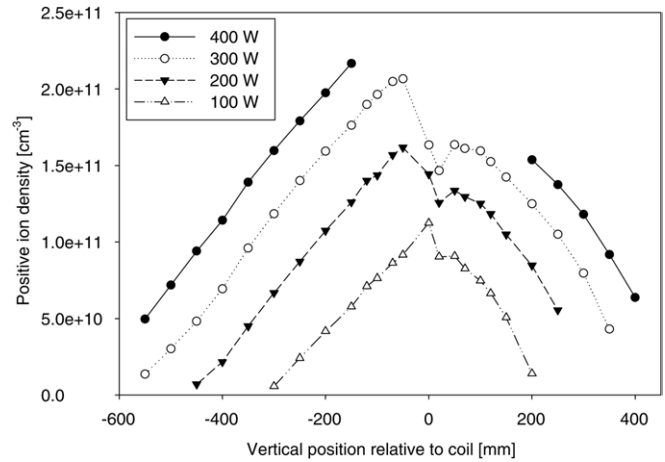


Figure 12. Axial positive ion density profiles as a function of the plasma power for a pressure of 200 Pa, a molar oxygen fraction of 33.3% and a total gas flow rate of 1500 sccm.

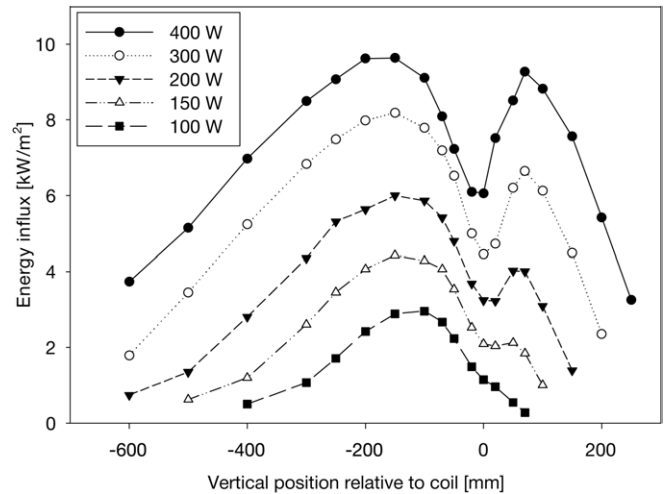


Figure 13. Axial energy influx profiles as a function of the plasma power for a pressure of 200 Pa, a molar oxygen fraction of 33.3% and a total gas flow rate of 1500 sccm.

of the ion density profile, discussed in the previous subsection, was much more pronounced at increased plasma power and nearly disappeared at the lowest power of 100 W. In the photographs in figure 10 the intense emission near the walls was also more pronounced at elevated power levels, indicating secondary electron emission. The high current γ -regime is normally concomitant with a low plasma density in the zone behind the sheath region [43], which behaves similarly to a Faraday dark space in a direct current glow discharge. We therefore suppose that the high current γ -configuration was preferably established at increased plasma power and led to the local drop in the positive ion density profile in the domain of the inductive coil.

The applied plasma power also had an influence on the axial energy influx profiles, shown in figure 13. The energy influx rose with increasing plasma power and reached a maximum of nearly 10 kW m^{-2} at a plasma power of 400 W. In addition, a higher expansion of the discharge in the glass tube is perceivable. At elevated plasma power, more radicals, charged and excited species are formed in the discharge. Thus,

a higher energy influx can be expected based on the higher frequency of recombination, association or impact processes on the surface of the calorimetric probe. The presented energy influx profiles in figure 13 agree well with the measurements in our earlier study in the afterglow of the TPR [22], where also an increased energy influx was found with rising plasma power. The absolute values were higher in [22], but this is most probably related to the different electrode configurations in the two experiments, which hamper a direct comparison.

The energy influx profiles at elevated plasma power also showed a local minimum in the region of the inductive coil, which became more pronounced with increasing plasma power. At the lowest discharge power of 100 W, a rather symmetric profile was measured with its maximum around 100 mm downstream of the inductive coil. Beginning at 150 W a plateau developed, and at a discharge power of 200 W a clear local minimum could be observed. According to our working hypothesis the local minimum in the energy influx profile developed because of two main reasons: on the one hand, the ion density along the central axis was reduced in the region of the helical coil, due to a transition from an α -like configuration to a plasma regime with similarities to a γ -configuration. This reduced locally the energy influx due to impinging ions and recombination reactions. On the other hand, the wall temperature increased with rising plasma power. This led most probably to an increased number of association reactions of oxygen radicals to O_2 at the reactor wall in this region. Hence, the energy influx due to association reactions of oxygen radicals was reduced at elevated plasma power, leading to this pronounced drop in the energy influx profile.

As already observed before, the energy influx profiles are shifted downstream compared with the profiles of electron temperature and ion density. The highest energy influx was measured approximately 100 to 200 mm downstream of the coil position. This effect is studied and discussed in more detail in the following subsection.

3.4. Mean gas velocity and residence time

The influence of the flow field and the mean gas velocity on the energy influx profiles was studied in a separate experimental series by varying the total gas flow rate at constant pressure. The effect on the spatial distribution of the optical emission is illustrated in figure 14. The mean gas velocities are calculated based on the gas flow rates by applying the ideal gas law and directly indicated in the photographs.

The variation of the mean gas velocity primarily influenced the expansion of the discharge and altered the axial and radial emission profiles. At the lowest gas flow rate the emission was very symmetrical with respect to the position of the inductive coil and emission near the wall was observed only in the domain of the coil. With increasing gas flow rate, the discharge expanded less upstream. In addition, the necking of the emission above the coil was reduced at elevated gas velocities, most probably due to a reduced number of negative ions, which were formed and transported towards the tube axis in this very short time. The highest expansion downstream of the coil was reached between velocities of 10 and 20 $m s^{-1}$.

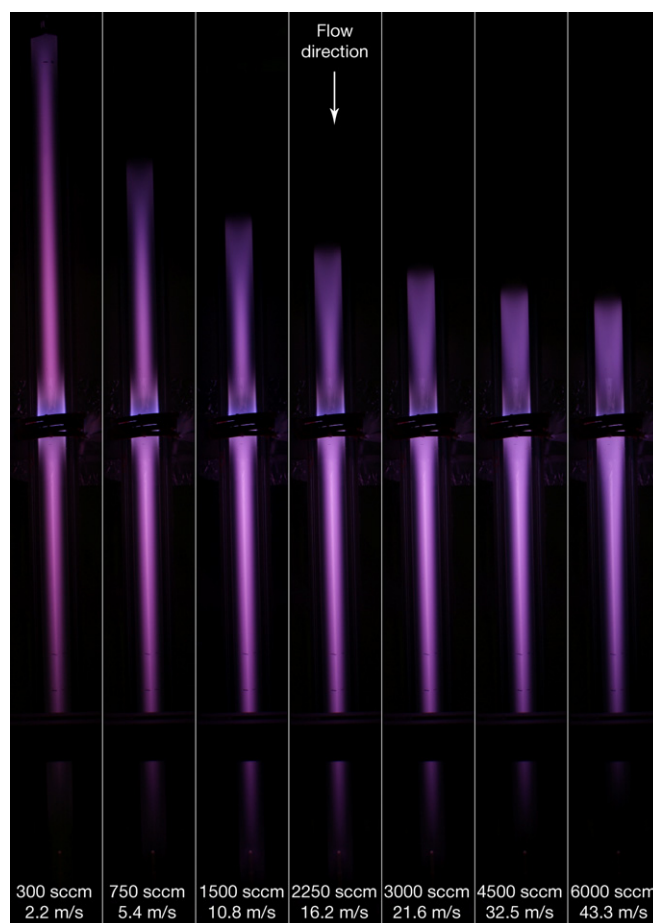


Figure 14. Photographs of the discharge as a function of the total gas flow rate for a plasma power of 300 W, a pressure of 200 Pa and a molar oxygen fraction of 33.3%. Photographs were taken with an aperture of 5 and an exposure time of 0.6 s.

At lower gas velocities the uncharged species may have lost their energy already at positions closer to the coil. At higher velocities the enhanced radial dispersion could have intensified loss mechanisms with the reactor wall.

The axial energy influx profiles, shown in figure 15, are shifted downstream with rising mean gas velocity. An increased energy influx in the afterglow of the TPR at elevated gas velocities was already found in our previous study at low discharge power [22]. We relate this shift mainly to the contribution of uncharged species which are not influenced by the electromagnetic fields and the negative wall charge but depend on the flow pattern and thus, on the mean gas velocity. Afterglow investigations of an oxygen discharge showed that the half-life of oxygen radicals measures several tens of milliseconds [51] and the density of neutral oxygen atoms in moderate pressure Ar:O₂ plasmas can exceed the plasma density by up to one order of magnitude [52]. Considering that a fluid element passes a length of 250 mm in approximately 5 ms at a mean gas velocity of 43.3 $m s^{-1}$, a high radical concentration can be expected in the afterglow. Hence, the downstream shift with increasing flow rates can be understood, by assuming that long-living ions and especially neutral species dominate the heating of the calorimetric probe in the afterglow.

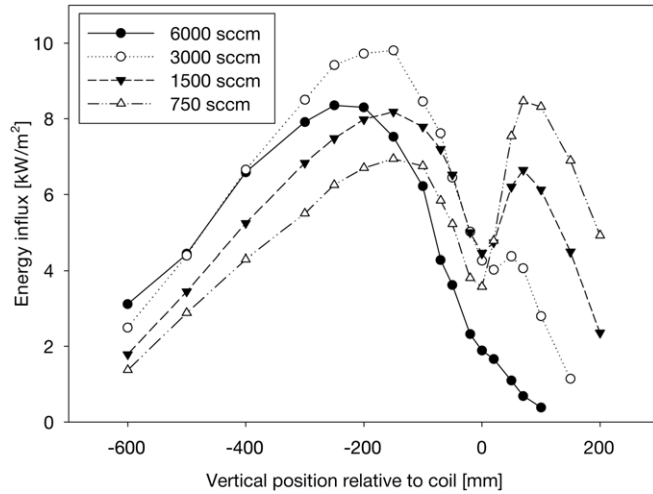


Figure 15. Axial energy influx profiles as a function of the total gas flow rate for a plasma power of 300 W, a pressure of 200 Pa and a molar oxygen fraction of 33.3%.

At low flow rates a strong local minimum in the profile developed and the highest energy influx was measured above the coil position. At a total gas flow rate of 1500 sccm the maximum energy influx was found downstream of the coil position. Still, a prominent minimum in the domain of the coil could be observed. At 3000 sccm the peak upstream of the coil nearly disappeared while the peak downstream of the helical coil became more pronounced. At the highest gas flow rate of 6000 sccm no local minimum was measured anymore and the maximum energy influx was located about 250 mm downstream of the coil position.

At elevated gas flow rates the same plasma power was distributed to more gas particles. Therefore, the mean energy of the particles was lower, causing a reduced neutral gas temperature. In addition, the emission near the wall seems reduced at elevated mean gas velocities in figure 14, indicating a lower secondary electron emission. Hence, we suppose that the heating of the wall was reduced at increased total gas flow rates. Under such conditions the heating process was probably dominated by volume processes as in an α -configuration CCP. This supports our hypothesis of the hot wall being partially responsible for the local minimum in the energy influx profiles. Overall, the obtained results at high gas velocities prove that the gas velocity has to be treated as an important process parameter in plasma chambers featuring moderate pressures and high gas flow rates.

3.5. Gas pressure

Several possibilities exist to study the influence of the gas pressure by varying process conditions. However, it is not possible to treat the process pressure as an independent variable. Both parameter variation series, described in section 2.1, were examined and photographs of the discharges are shown in figure 16.

At low-pressure levels the discharge expands further up- and downstream with respect to the coil position in both series. The number of collisions rose with increasing pressure

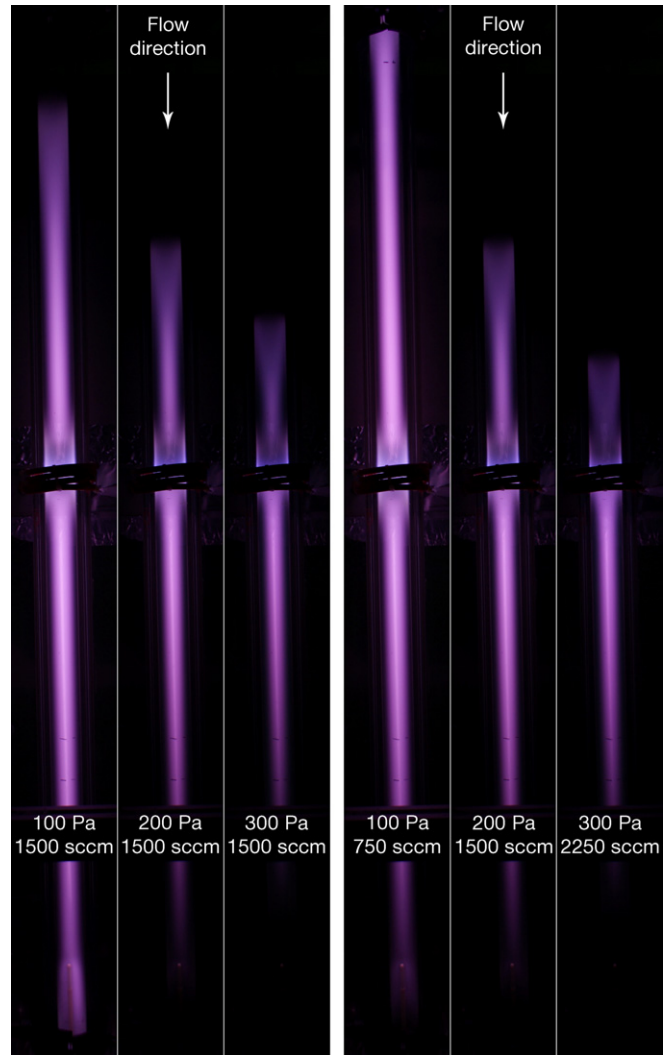


Figure 16. Photographs of the discharge as a function of the pressure for a plasma power of 300 W and a molar oxygen fraction of 33.3%. Left series: constant specific energy input per gas particle, right series: constant residence time. Photographs were taken with an aperture of 5 and an exposure time of 0.6 s.

and thus, the mean free path of excited or charged species decreased. In the left series with constant gas flow rate the mean gas velocity doubled from 10.8 to 21.6 m s^{-1} by lowering the pressure from 200 to 100 Pa. Therefore, the discharge expanded far downstream but did not reach the upper flange. In contrast, the discharge expanded upwards into the flange but was confined inside the glass tube downstream in the respective discharge at 100 Pa where the mean gas velocity was kept constant (right series). Likewise, the discharge expanded less upstream at 300 Pa, if the gas flow rate was adjusted (right series), compared with the case if the total gas flow rate was kept constant (left series).

Langmuir double probe measurements in the zone around the inductive coil were limited to an upper pressure in the order of 200 Pa. At 300 Pa the probe tips heated up substantially and the inaccuracies became unacceptably large. In contrast, the calorimetric technique was not limited to the regions up- and downstream of the coil, but the whole profiles along the reactor axis could be acquired, as presented in figure 17. In both

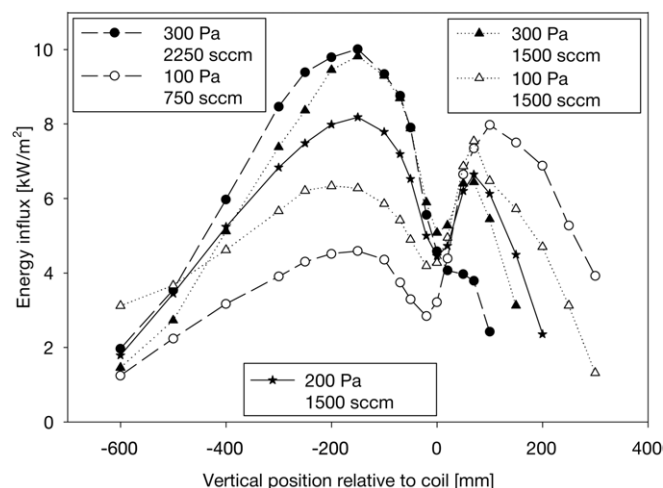


Figure 17. Axial energy influx profiles as a function of the pressure for a plasma power of 300 W and a molar oxygen fraction of 33.3%.

series the maximum energy influx rose with increasing process pressure, where more collisions between charged and excited particles with neutrals in the ground state occurred. This limited the expansion of the afterglow and led to a short but intense discharge at elevated pressure.

An increased mean gas velocity shifted the energy influx profiles downstream, as already shown in figure 15. A variation of the system pressure with constant gas flow rate (triangles in figure 17) demonstrated therefore the effect of changing the two parameters, pressure and mean gas velocity, simultaneously. A lower pressure not only led to an expansion of the discharge but the maximum energy influx was also shifted downstream due to the higher mean gas velocity. On the other hand, the discharge was contracted and the uncharged species were transported slower to the lower section of the tube at elevated pressures and low mean gas velocities. In the second series with constant residence time (spheres in figure 17) the profiles were not influenced by a varying mean gas velocity but the specific energy input per gas particle was not constant throughout the series. Comparing the two profiles at 100 Pa it can be noticed that the energy influx above the coil position was higher in the case where the residence time was kept constant (spheres). The increased mean gas velocity in the other series (triangles) transported more metastables and radicals downstream which led to an increased energy influx below the coil position at the same pressure level.

Again, all profiles featured a local reduction of the energy influx in the region of the inductive coil. The local minimum was less pronounced at increased process pressure and nearly disappeared by increasing the pressure to 300 Pa in series with constant residence time. In general, the sheath thickness decreases with rising pressure in the discharge [53]. In the photographs shown in figure 16 the luminous region near the wall in the domain of the coil was less pronounced at 300 Pa compared with the lower pressure series. This suggests a reduced secondary electron emission at higher pressure levels. Thus, the discharge featured more α -mode properties, where the heating of the wall was reduced compared with conditions where the plasma was sustained primarily by

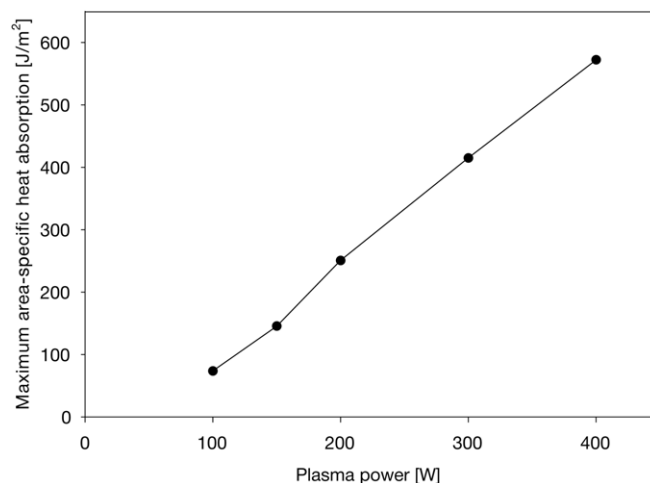


Figure 18. Maximum area-specific energy absorption as a function of the plasma power for a pressure of 200 Pa, a molar oxygen fraction of 33.3% and a total gas flow rate of 1500 sccm.

secondary electron emission at the wall. We therefore assume that a reduced wall heating in the domain of the inductive coil was responsible for the less pronounced local minimum in the energy influx profile at elevated pressure levels.

The shorter but more intense plasma at increased pressures can be advantageous for several applications of the TPR. The discharge can be operated in a confined mode even at high plasma power if the process is run at an elevated pressure. In a previous study it was additionally found that nanoparticles are preferably formed from organosilicon monomers at increased process pressure. Under these conditions, the synthesized nanoparticles featured a high degree of oxidation and more particles were formed per time [54].

3.6. Thermal load of substrate particles immersed to the plasma

The energy absorption of a substrate particle during the surface modification is proportional to the integral of the energy influx along its path through the reactor. In our earlier studies we showed that the energy influx reaches its maximum in the central axis of the reactor [20,22]. Thus, we calculated the maximum area-specific energy absorption by integrating the energy influx profiles according to the respective residence time. For the numerical integration of the axial profiles we applied the trapezoidal rule.

In figure 18 the integrated energy influx is shown for the power series of figure 13. Even though the energy influx measurements themselves own a certain error and the integration adds some uncertainty the trend is clear and comprehensible: the maximum area-specific energy, which is absorbed by any insulated substrate passing the reactor, increases with plasma power.

The oxygen fraction of the process gas had nearly no influence on the integrated energy influx, shown in figure 19, and values between 374 and 423 J m⁻² were obtained. Interestingly, even the H-mode plasma in pure argon lead to a comparable energy absorption as the E-mode discharges in the case of Ar : O₂ mixtures or pure oxygen.

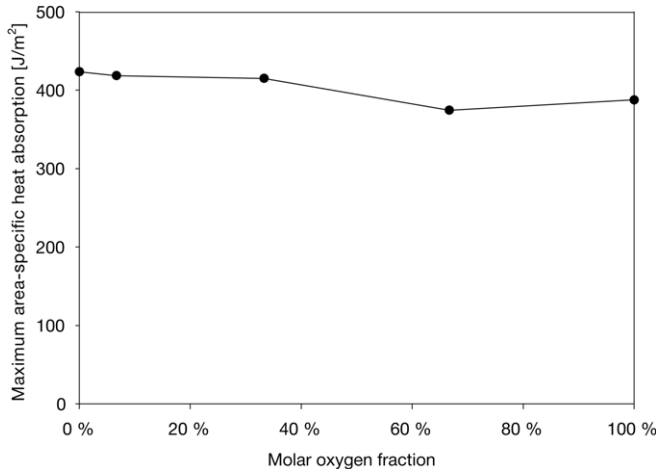


Figure 19. Maximum area-specific energy absorption as a function of the molar oxygen fraction for a plasma power of 300 W, a pressure of 200 Pa and a total gas flow rate of 1500 sccm.

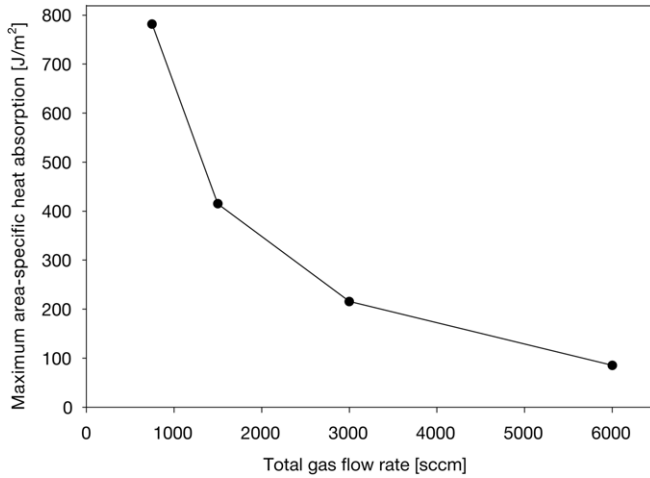


Figure 20. Maximum area-specific energy absorption as a function of the total gas flow rate for a plasma power of 300 W, a pressure of 200 Pa and a molar oxygen fraction of 33.3%.

In figure 20 the maximum area-specific energy absorption is shown as a function of the mean gas velocity. Even though the maximum energy influx values shown in figure 15 were comparable within the series, the integrated energy influx decreases strongly with increasing total gas flow rate. Assuming that a substrate particle follows the flow pattern, it passes the plasma zone much faster at increased gas flow rates. Therefore, the varying residence time is responsible for the curve propagation in figure 20.

The fourth parameter affecting the maximum area-specific energy absorption is the process pressure. As already discussed in section 3.5, the pressure cannot be varied independently. Therefore, again both series with either constant mean gas velocity or constant total gas flow rate are shown in figure 21.

The integrated energy influx does not increase significantly with pressure, if the mean gas velocity is kept constant (adjusting the total gas flow rate). Nevertheless, an increased energy absorption with rising pressure can be noticed in the second series with a constant total gas flow rate. In this series a variation of the pressure had a direct influence on the mean

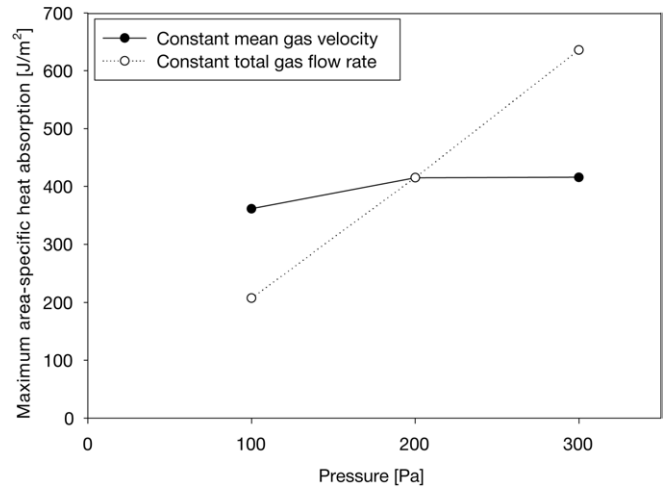


Figure 21. Maximum area-specific heat absorption as a function of the pressure for a plasma power of 300 W and a molar oxygen fraction of 33.3%.

gas velocity and thus, on the residence time. Hence, it is not primarily the pressure which determines the maximum absorbed energy, but rather the residence time of a substrate within the discharge.

In reality the absorbed area-specific energy of a particle is lower than the values stated above. On the one hand, it is improbable that a particle exactly follows a streamline along the central axis through the reactor. On the other hand, the discharge characteristics alter significantly if large amounts of powder are fed to the reactor. The powder provides a very high specific surface onto which the energy flux is distributed. Above a certain specific surface the available power cannot countervail the numerous losses and thus, the energy influx decreases. Hence, the values stated in figures 18–22 should be regarded as the maximum limit of heat absorption for the idealized case of an undisturbed discharge.

A particle does not only absorb heat, but loses energy by convection and radiation as well. Hence, the axial energy influx profile in combination with the different loss mechanisms defines the maximum transient particle temperature $T_{p,max}(t)$ during the treatment. Numerical calculations of the transient particle temperature are possible. However, several assumptions concerning the inner wall temperature, gas temperature, and particle properties are necessary. The transient particle temperature within a spherical particle of radius r_p is governed by the heat equation in radial coordinates (8).

$$\frac{\partial T_p}{\partial t} = \frac{\lambda_p}{\rho_p \cdot c_{p,p}} \cdot \frac{1}{r^2} \cdot \frac{1}{\partial r} \left(r^2 \cdot \frac{\partial T_p}{\partial r} \right), \quad (8)$$

where λ_p is the thermal conductivity, ρ_p is the density and $c_{p,p}$ is the specific heat capacity of the particle. In order to solve this equation, an initial condition and two boundary conditions are necessary. As initial condition (9) we assume that the particle owns a uniform temperature T_0 .

$$T_p(r, 0) = T_0. \quad (9)$$

Table 3. Known and estimated parameters for the particle temperature calculation.

Parameter	Symbol	Value	Reference
Thermal conductivity of lactose	λ_p	$1 \text{ W m}^{-1} \text{ K}^{-1}$	Estimated
Specific heat capacity of lactose at 25 °C	$c_{p,p}$	$1210 \text{ J kg}^{-1} \text{ K}^{-1}$	[56]
Density of lactose	ρ_p	1520 kg m^{-3}	[57]
Initial temperature	T_0	20°C	Estimated
Maximum wall temperature	$T_{\text{wall,max}}$	50°C	Estimated
Maximum gas temperature	$T_{\text{gas,max}}$	80°C	Estimated
Emissivity	e	0.8	Estimated
Mean gas velocity	v_{mean}	10.8 m s^{-1}	Calculated
Mean free path at 200 Pa (1/3 O ₂ , 2/3 Ar)	λ_{mfp}	$3.9 \times 10^{-5} \text{ m}$	Calculated
Thermal accommodation coefficient	α_{ac}	0.8	Estimated
Thermal conductivity of the gas at 200 Pa,	λ_{gas}	0.02145	[58]

We suppose spherical symmetry within the particle such that no heat is conducted through the particle centre. This is the first boundary condition (10).

$$-\lambda_p \cdot \frac{\partial T_p}{\partial r} \Big|_{r=0} = 0. \quad (10)$$

The second boundary condition (11) at the particle surface connects the heat transfer between the particle and its surrounding with the heat conduction inside the particle.

$$-\lambda_p \cdot \frac{\partial T_p}{\partial r} \Big|_{r=r_p} = J_{\text{in}}(t) - \alpha_c \cdot (T_p(r_p, t) - T_{\text{gas}}(t)) - \sigma_s \cdot \varepsilon \cdot (T_p(r_p, t)^4 - T_{\text{wall}}(t)^4), \quad (11)$$

where α_c is the convective heat transfer coefficient, σ_s is the Stefan–Boltzmann constant and ε is the emissivity. The heat loss terms by convection and radiation depend on the unknown inner wall temperature T_{wall} and the unknown gas temperature T_{gas} . These temperatures vary along the axial position x within the reactor, which was transferred to the time space according to the mean gas velocity v_{mean} (12). The time 0 relates to the point where the particle enters the discharge and t_{res} refers to the residence time, after which the particle leaves the plasma.

$$x = v_{\text{mean}} \cdot t \quad t[0 \dots t_{\text{res}}]. \quad (12)$$

Since the propagation of both temperatures T_{wall} and T_{gas} were unknown, their profiles were estimated to follow the energy influx profile as shown in (13) and (14). The maximum inner wall temperature $T_{\text{wall,max}}$ under standard process conditions was estimated to be 50°C based on an energy balance including the cooling water in- and outlet temperatures and standard correlations for the heat transfer through a tube. The gas temperature is a strong function of the wall temperature at high surface-to-volume ratios. Thus, we assume that $T_{\text{gas,max}}$ is only slightly higher than $T_{\text{wall,max}}$.

$$T_{\text{wall}}(t) = (T_{\text{wall,max}} - T_0) \cdot \frac{J_{\text{in}}(t)}{J_{\text{in,max}}} + T_0 \quad (13)$$

$$T_{\text{gas}}(t) = (T_{\text{gas,max}} - T_0) \cdot \frac{J_{\text{in}}(t)}{J_{\text{in,max}}} + T_0. \quad (14)$$

While the loss by radiation is generally rather low at the investigated temperatures and only the emissivity has to be estimated, a higher uncertainty is related to the convective

loss. Neither the correlations for the continuum regime nor those for the free molecular regime can be applied in the investigated pressure range. In the intermediate regime, correlations including corrections by the Knudsen number Kn should be used. Kn relates the mean free path λ_{mfp} of the neutral gas particles to the characteristic distance, which is in our case the particle diameter d_p (15).

$$Kn = \frac{\lambda_{\text{mfp}}}{d_p} = \frac{1}{d_p \cdot n \cdot \sigma}. \quad (15)$$

The mean free path can be calculated by the number density n and the collision cross-section σ . At a pressure of 200 Pa, the Knudsen number varies from about 39 to 0.078 for particle diameters ranging from 1 to $500 \mu\text{m}$. Hence, for each particle diameter the convective heat transfer coefficient α_c can be calculated using a suitable Nusselt correlation, as the one presented in (16) for the heat transfer from a sphere to a rarefied gas mixture [55].

$$Nu = \frac{\alpha_c \cdot d_p}{\lambda_{\text{gas}}} = \frac{2}{1 + 7.5 \cdot \alpha_{\text{ac}}^{-1} \cdot Kn}, \quad (16)$$

where λ_{gas} is the thermal conductivity of the gas mixture and α_{ac} is the thermal accommodation coefficient. Even though, the calculation of the transient particle temperature depends on many assumptions, we exemplarily estimated the temperature propagation for the energy influx profile measured under standard process conditions and lactose as the substrate material. All known and estimated parameters are summarized in table 3. The heat equation was solved with a radial and temporal resolution of 200 steps and for particle diameters ranging from 0.5 to $600 \mu\text{m}$.

The maximum temperatures were always reached at $r = r_p$. The radial temperature differences within the particles were small ($<0.5 \text{ K}$) since the thermal conductivity was high enough to equilibrate temperature differences within the particle very fast. The calculated transient temperature propagation at the particle surface ($r = r_p$) is shown for several particle diameters in figure 22.

Small particles feature a very high surface-to-volume ratio and follow, according to the simulation, the propagation of the local energy influx and gas temperature. With increasing particle size the heat capacity of the particles rises and the interaction with the surrounding gas is less dominant. Above a

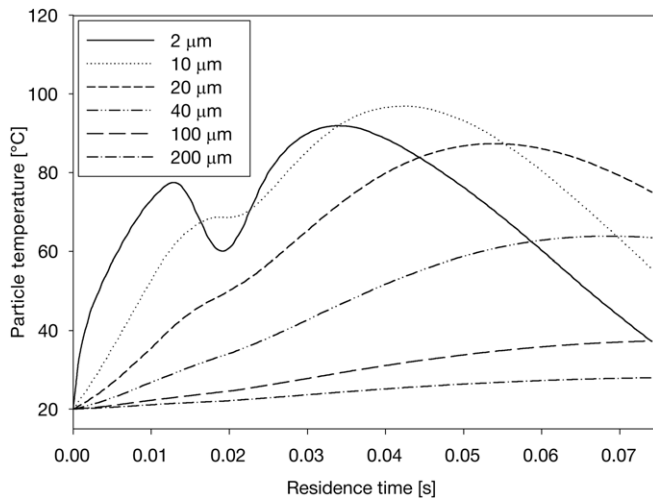


Figure 22. Simulated transient particle surface temperature of lactose particles with various diameters passing the discharge under standard process conditions.

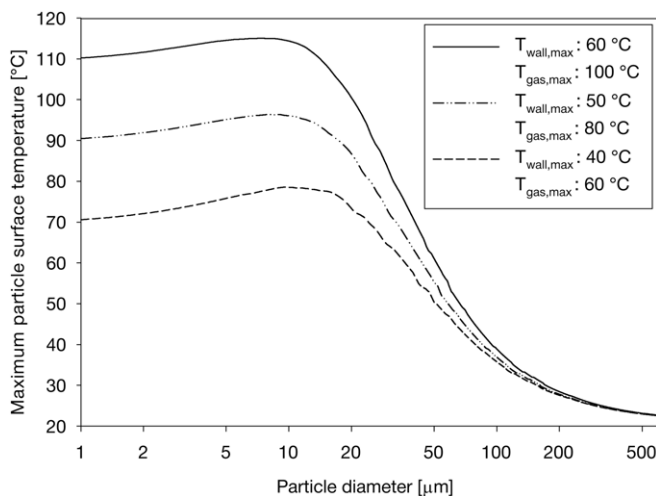


Figure 23. Simulated maximum particle surface temperatures of lactose particles passing the discharge under standard process conditions as a function of the particle diameter.

particle diameter of approximately $40\text{ }\mu\text{m}$ the energy influx due to the plasma J_{in} is higher than the convective loss during the whole treatment time. Therefore, the maximum temperature is reached at $t = t_{\text{res}}$, when the particle leaves the discharge at the lower end of the tube. The energy influx and the loss terms are proportional to r^2 , but the heat capacity is proportional to r^3 . Thus, the heating reduces further with rising particle size and becomes exiguous for particle diameters of several hundred micrometres and above. The maximum particle temperature is reached at the vertical position where J_{in} is at its maximum or further downstream.

In figure 23 the maximum of the transient particle temperature is plotted as a function of the particle diameter. According to the simulation, particles with a diameter in the order of $10\text{ }\mu\text{m}$ reach the maximum temperature. Smaller particles are able to dissipate a lot of energy by convection, while larger particles heat up slower due to their higher heat capacity.

In addition to the specified maximum gas and wall temperatures in table 3, also higher and lower estimates were used for the simulation and shown in figure 23. The influence of the gas temperature is rather high, especially for small particles. Therefore, the maximum possible particle temperature can only be approximated in the order of $100\text{ }^\circ\text{C}$.

Even though the presented maximum temperature is calculated for the ideal case of unaffected plasma characteristics at low powder concentrations and particles following the central axis of the TPR, the risk for thermal product damage cannot be neglected. Powders with melting points below $100\text{ }^\circ\text{C}$ are at risk for melting or degradation and should be processed at low plasma power or short residence time. On the other hand, more resistant powders, such as lactose with a melting point of $201\text{ }^\circ\text{C}$, should not be endangered under standard process conditions.

In general the following statements can be made: if a high degree of surface modification is required and substrate heating is not critical, the process should be run at high powers, high pressures and low total gas flow rates. In contrast, temperature sensitive materials are preferably modified at increased mean gas velocities or reduced plasma power, if the degree of surface functionalization can be reached under such conditions. The gas composition has only a minor influence on the expected particle temperature.

4. Conclusions

The tubular plasma reactor is designed for the continuous surface modification of fine-grained powder substrates. The key piece of this system is a glass tube of 1.5 m length and an inner diameter of 40 mm . In this glass tube a non-equilibrium discharge is sustained to modify particles passing the tube with high velocity. No powder was fed in this study but pure argon–oxygen mixtures flowed through the tube with mean gas velocities between 2 and 43 m s^{-1} at pressure levels between 100 and 300 Pa . Langmuir double probe and calorimetric probe measurements were performed to provide axial profiles of electron temperature, positive ion density, and energy influx as a function of the process parameters. These profiles are required to explain the on-going processes during the particle surface modification and to develop new functionalization routes under preferable plasma conditions. In addition, photographs of the plasma are presented to explain the characteristic differences between the discharges under various process conditions.

A new type of calorimetric probe is introduced which consists of a ceramic probe head with known heat capacity, an internal fibre optic temperature sensor, and a ceramic rod to withstand high energy influxes up to 50 kW m^{-2} , strong electromagnetic fields, and the oxidizing environment in the investigated Ar:O₂ discharge.

Even though the power was coupled to the discharge by an inductive coil on the outside of the glass tube, the capacitive E-mode was established under process conditions which are normally chosen for powder processing. Different discharge regimes with either volume dominated heating (α -mode) or strong secondary electron emission (γ -mode) were identified

along the tube axis. The maximum electron temperature was found in the domain of the inductive coil and decreased up- and downstream. In the discharge centre high values up to 17 eV have been found. The axial profile of the positive ion density showed a similar propagation as the electron temperature and decreased towards the upper and lower flange of the glass tube. Maximum positive ion densities in the order of $2 \times 10^{11} \text{ cm}^{-3}$ were determined and the density rose with increasing plasma power. The energy influx rose as well with increasing plasma power but was additionally strongly influenced by the flow field. At elevated mean gas velocities the energy influx profile was shifted downstream. Excited and dissociated neutrals are not deflected by the electromagnetic fields and feature long lifetimes. We therefore assume that uncharged species are responsible for the measured energy influx maxima downstream of the discharge centre.

In a certain range of process parameters a pronounced local minimum in the positive ion density and energy influx profile was found at the axial position of the inductive coil. In the ion density profile this local density reduction was attributed to an α - γ -mode transition, known from capacitive discharges at moderate pressures. In the energy influx profile, the effect of the local wall temperature on the measured profiles is discussed and considered as a potential explanation for the local drop in energy influx.

The energy influx is an integral parameter, representing the sum of all energetic particle fluxes towards the probe as well as surface reactions. Thus, statements about the thermal load that a substrate would encounter during the exposure in this environment are possible. We integrated the axial energy influx profiles numerically with respect to residence time. The resulting values are proportional to the thermal load of a substrate particle passing the discharge under such conditions. Based upon this calculation a maximum thermal load is expected at high plasma power and low mean gas velocity. We also simulated the transient particle temperature by including heat loss terms into the calculation. According to this simulation a maximum particle temperature in the order of 100 °C is expected for powders similar to lactose. Hence, the presented profiles and calculations will help to assess the risk of powder melting in the current reactor and even more, assist in choosing appropriate process parameters for a specific surface functionalization in future.

Acknowledgment

Financial support from Claude & Giuliana Foundation (Switzerland) is gratefully acknowledged.

References

- [1] Roth C, Künsch Z, Sonnenfeld A and Rudolf von Rohr P 2011 Plasma surface modification of powders for pharmaceutical applications *Surf. Coat. Technol.* **205** S597–600
- [2] Borer B and Rudolf von Rohr P 2005 Growth structure of SiO_x films deposited on various substrate particles by PECVD in a circulating fluidized bed reactor *Surf. Coat. Technol.* **200** 377–81
- [3] Arpagaus C, Rossi A and Rudolf von Rohr P 2005 Short-time plasma surface modification of HDPE powder in a plasma downer reactor—process, wettability improvement and ageing effects *Appl. Surf. Sci.* **252** 1581–95
- [4] Roth C, Keller L and Rudolf von Rohr P 2012 Adjusting dissolution time and flowability of salicylic acid powder in a two stage plasma process *Surf. Coat. Technol.* **206** 3832–8
- [5] Arpagaus C, Sonnenfeld A and Rudolf von Rohr P 2005 A downer reactor for short-time plasma surface modification of polymer powders *Chem. Eng. Technol.* **28** 87–94
- [6] Hopwood J 1992 Review of inductively coupled plasmas for plasma processing *Plasma Sources Sci. Technol.* **1** 109–16
- [7] Kortshagen U, Gibson N D and Lawler J E 1996 On the E–H mode transition in RF inductive discharges *J. Phys. D: Appl. Phys.* **29** 1224–36
- [8] Johnson E O and Malter L 1950 A floating double probe method for measurements in gas discharges *Phys. Rev.* **80** 58–68
- [9] Annaratone B M, Counsell G F, Kawano H and Allen J E 1992 On the use of double probes in RF discharges *Plasma Sources Sci. Technol.* **1** 232–41
- [10] Chen F F 1965 *Plasma Diagnostic Techniques* ed R H Huddleston and S L Leonard (New York: Academic) pp 113–200
- [11] Brockhaus A, Borchardt C and Engemann J 1994 Langmuir probe measurements in commercial plasma plants *Plasma Sources Sci. Technol.* **3** 539–44
- [12] Thornton J A 1978 Substrate heating in cylindrical magnetron sputtering sources *Thin Solid Films* **54** 23–31
- [13] Kersten H, Deutsch H, Steffen H, Kroesen G M W and Hippler R 2001 The energy balance at substrate surfaces during plasma processing *Vacuum* **63** 385–431
- [14] Kersten H, Stoffels E, Stoffels W W, Otte M, Csambal C, Deutsch H and Hippler R 2000 Energy influx from an RF plasma to a substrate during plasma processing *J. Appl. Phys.* **87** 3637–45
- [15] Wendt R, Ellmer K and Wiesemann K 1997 Thermal power at a substrate during ZnO: Al thin film deposition in a planar magnetron sputtering system *J. Appl. Phys.* **82** 2115–22
- [16] Quitzau M and Kersten H 2012 Determination of electron density and energy influx in a hollow cathode glow discharge used for powder modification *Eur. Phys. J. D* **66** 47
- [17] Bornholdt S, Wolter M and Kersten H 2010 Characterization of an atmospheric pressure plasma jet for surface modification and thin film deposition *Eur. Phys. J. D* **60** 653–60
- [18] Swinkels G, Kersten H, Deutsch H and Kroesen G M W 2000 Microcalorimetry of dust particles in a radio-frequency plasma *J. Appl. Phys.* **88** 1747–55
- [19] Maurer H R and Kersten H 2011 On the heating of nano- and microparticles in process plasmas *J. Phys. D: Appl. Phys.* **44** 174029
- [20] Roth C, Spillmann A, Sonnenfeld A and Rudolf von Rohr P 2009 Thermal characterization and optimization of a plasma downstream reactor for particle surface modification *Plasma Process. Polym.* **6** S566–70
- [21] Stahl M, Trottenberg T and Kersten H 2010 A calorimetric probe for plasma diagnostics *Rev. Sci. Instrum.* **81** 023504
- [22] Roth C, Bornholdt S, Zuber V, Sonnenfeld A, Kersten H and Rudolf von Rohr P 2011 Comparison of calorimetric plasma diagnostics in a plasma downstream reactor *J. Phys. D: Appl. Phys.* **44** 095201
- [23] Lee M H, Lee K H, Hyun D S and Chung C W 2007 On the hysteresis in E to H and H to E transitions and the multistep ionization in inductively coupled plasma *Appl. Phys. Lett.* **90** 191502
- [24] Annaratone B M, Allen M W and Allen J E 1992 Ion currents to cylindrical Langmuir probes in RF plasmas *J. Phys. D: Appl. Phys.* **25** 417–24

- [25] Klagge S and Tichy M 1985 A contribution to the assessment of the influence of collisions on the measurements with Langmuir probes in the thick sheath working regime *Czech. J. Phys.* **35** 988–1006
- [26] David P, Sicha M, Tichy M, Kopiczynski T and Zakrzewski Z 1990 The use of Langmuir probe methods for plasma diagnostic in middle pressure discharges *Contrib. Plasma Phys.* **30** 167–84
- [27] Kirchhoff R H, Peterson E W and Talbot L 1971 An experimental study of the cylindrical Langmuir probe response in the transition regime *AIAA J.* **9** 1686–94
- [28] Amemiya H 1988 Characteristics of double probe in negative ion-containing plasmas *Japan. J. Appl. Phys. Part 1—Regul. Pap. Short Notes Rev. Pap.* **27** 2423–4
- [29] Amemiya H 1990 Plasmas with negative-ions—probe measurements and charge equilibrium *J. Phys. D: Appl. Phys.* **23** 999–1014
- [30] Kim S, Lieberman M A, Lichtenberg A J and Gudmundsson J T 2006 Improved volume-averaged model for steady and pulsed-power electronegative discharges *J. Vac. Sci. Technol. A* **24** 2025–40
- [31] Morscheidt W, Hassouni K, Bauduin N, Arefi-Khonsari F and Amouroux J 2003 On the use of global kinetics models for the investigation of energy deposition and chemistry in RF argon–oxygen plasmas working in the torr regime *Plasma Chem. Plasma Process.* **23** 117–40
- [32] White G K and Minges M L 1997 Thermophysical properties of some key solids: an update *Int. J. Thermophys.* **18** 1269–327
- [33] Thurmond C D 1975 Standard thermodynamic functions for formation of electrons and holes in Ge, Si, GaAs, and GaP *J. Electrochem. Soc.* **122** 1133–41
- [34] Corr C S, Steen P G and Graham W G 2003 Instabilities in an inductively coupled oxygen plasma *Plasma Sources Sci. Technol.* **12** 265–72
- [35] Katsch H M, Sturm T, Quandt E and Dobelev H F 2000 Negative ions and the role of metastable molecules in a capacitively coupled radiofrequency excited discharge in oxygen *Plasma Sources Sci. Technol.* **9** 323–30
- [36] Schwabedissen A, Soll C, Brockhaus A and Engemann J 1999 Electron density measurements in a slot antenna microwave plasma source by means of the plasma oscillation method *Plasma Sources Sci. Technol.* **8** 440–7
- [37] Wagatsuma K and Hirokawa K 1995 Effect of oxygen addition to an argon glow-discharge plasma source in atomic emission spectrometry *Anal. Chim. Acta* **306** 193–200
- [38] Schmidt M and Conrads H 2008 *Low Temperature Plasmas: Fundamentals, Technologies, and Techniques* vol 1, ed R Hippler *et al* (Weinheim: Wiley) pp 363–83
- [39] Kousal J, Tichy M, Sebek O, Cechvala J and Biederman H 2011 Langmuir probe study of a magnetically enhanced RF plasma source at pressures below 0.1 Pa *Plasma Sources Sci. Technol.* **20** 6
- [40] Amorim J, Maciel H S and Sudano J P 1991 High-density plasma mode of an inductively coupled radio-frequency discharge *J. Vac. Sci. Technol. B* **9** 362–5
- [41] Gudmundsson J T and Thorsteinsson E G 2007 Oxygen discharges diluted with argon: dissociation processes *Plasma Sources Sci. Technol.* **16** 399–412
- [42] Raizer Y P, Shneider M N and Yatsenko N A 1995 *Radio-Frequency Capacitive Discharges* (Boca Raton, FL: CRC Press)
- [43] Lisovskiy V A and Yegorenkov V D 2004 Alpha-gamma transition in RF capacitive discharge in low-pressure oxygen *Vacuum* **74** 19–28
- [44] Piejak R, Godyak V, Alexandrovich B and Tishchenko N 1998 Surface temperature and thermal balance of probes immersed in high density plasma *Plasma Sources Sci. Technol.* **7** 590–8
- [45] Takechi K and Lieberman M A 2001 Effect of Ar addition to an O₂ plasma in an inductively coupled, traveling wave driven, large area plasma source: O₂/Ar mixture plasma modeling and photoresist etching *J. Appl. Phys.* **90** 3205–11
- [46] Pagnon D, Amorim J, Nahorny J, Touzeau M and Vialle M 1995 On the use of actinometry to measure the dissociation in O₂ DC glow-discharges—determination of the wall recombination probability *J. Phys. D: Appl. Phys.* **28** 1856–68
- [47] Macko P, Veis P and Cernogora G 2004 Study of oxygen atom recombination on a Pyrex surface at different wall temperatures by means of time-resolved actinometry in a double pulse discharge technique *Plasma Sources Sci. Technol.* **13** 251–62
- [48] Sheridan T E, Chabert P and Boswell R W 1999 Positive ion flux from a low-pressure electronegative discharge *Plasma Sources Sci. Technol.* **8** 457–62
- [49] Sheridan T E 1999 Double layers in a modestly collisional electronegative discharge *J. Phys. D: Appl. Phys.* **32** 1761–7
- [50] Lieberman M A and Lichtenberg A J 2005 *Principles of Plasma Discharges and Materials Processing* (Hoboken, NJ: Wiley)
- [51] Brockhaus A, Leu G F, Selenin V, Tarnev K and Engemann J 2006 Electron release in the afterglow of a pulsed inductively-coupled radiofrequency oxygen plasma *Plasma Sources Sci. Technol.* **15** 171–7
- [52] Mozetic M, Vesel A, Cvelbar U and Ricard A 2006 An iron catalytic probe for determination of the O-atom density in an Ar/O₂ afterglow *Plasma Chem. Plasma Process.* **26** 103–17
- [53] Mutsukura N, Fukasawa Y, Machi Y and Kubota T 1994 Diagnostics and control of radiofrequency glow-discharge *J. Vac. Sci. Technol. A* **12** 3126–30
- [54] Roth C, Oberbessel G, Buitrago E, Heuberger R and Rudolf von Rohr P 2012 Nanoparticle synthesis and growth in a continuous plasma reactor from organosilicon precursors *Plasma Process. Polym.* **9** 119–34
- [55] Mikami H, Endo Y and Takashima Y 1966 Heat transfer from a sphere to rarefied gas mixtures *Int. J. Heat Mass Transfer* **9** 1435–48
- [56] Hernandez-Segura G O, Campos M, Costas M and Torres L A 2009 Temperature dependence of the heat capacities in the solid state of 18 mono-, di-, and poly-saccharides *J. Chem. Thermodyn.* **41** 17–20
- [57] Wong L W and Pilpel N 1990 The effect of particle-shape on the mechanical-properties of powders *Int. J. Pharm.* **59** 145–54
- [58] Lemmon E W, McLinden M O and Friend D G 2012 Thermophysical properties of fluid systems *NIST Chemistry WebBook, NIST Standard Reference Database* number 69, ed P J Linstrom and W G Mallard (Gaithersburg MD: National Institute of Standards and Technology)